Journal of
Synchrotron
Radiation

ISSN 0909-0495

Received 9 September 2009
Accepted 3 February 2010

Kinoform optics applied to X-ray photon correlation spectroscopy

A. R. Sandy,[a]* S. Narayanan,[a] M. Sprung,[a]‡ J.-D. Su,[a] K. Evans-Lutterodt,[b] A. F. Isakovic[b] and A. Stein[c]

[a]X-ray Science Division, Argonne National Laboratory, Argonne, IL 60439, USA, [b]National Synchrotron Light Source, Brookhaven National Laboratory, Upton, NY 11973, USA, and [c]Center for Functional Nanomaterials, Brookhaven National Laboratory, Upton, NY 11973, USA. E-mail: asandy@anl.gov

Moderate-demagnification higher-order silicon kinoform focusing lenses have been fabricated to facilitate small-angle X-ray photon correlation spectroscopy (XPCS) experiments. The geometric properties of such lenses, their focusing performance and their applicability for XPCS measurements are described. It is concluded that one-dimensional vertical X-ray focusing *via* silicon kinoform lenses significantly increases the usable coherent flux from third-generation storage-ring light sources for small-angle XPCS experiments.

Keywords: focusing hard X-rays; kinoform refractive optics; X-ray photon correlation spectroscopy (XPCS); X-ray intensity fluctuation spectroscopy (XIFS); X-ray speckle.

1. Introduction

X-ray photon correlation spectroscopy (XPCS) is the X-ray analogue of dynamic light scattering. It permits characterization of the equilibrium or steady-state dynamics of condensed matter on length scales shorter than can be achieved with optical techniques and on longer time scales than can be achieved *via* neutron scattering. Over the past several years the technique has matured scientifically; recent reviews provide a perspective (Livet, 2007; Sutton, 2008; Grübel *et al.*, 2008). Despite recent progress, however, the technique remains challenging because of relatively low signal levels even at third-generation synchrotron sources. As such, it remains critical to carefully optimize all aspects of XPCS experiments so that they are performed as effectively as possible. This article details one such optimization, namely vertical focusing, so that the full coherent flux delivered by an undulator at a third-generation storage-ring synchrotron source can be used in a small-angle XPCS experiment.

Because of the aforementioned low signal levels, area detectors are often used for XPCS experiments because the scattering signal can be simultaneously collected both from many different but equivalent wavevector transfers (Qs) and over a span of different Qs. Data collected simultaneously at equivalent Qs permit averaging of the autocorrelation functions thus improving statistics, while data collected simultaneously at different wavevectors greatly increases the efficiency of such experiments. For large collimating slit sizes, it has been shown (Falus *et al.*, 2006) that the signal-to-noise ratio (SNR) for a measured autocorrelation decay function is maximized when the angular extent of the detector pixels as seen from the sample position matches that of the source as seen from the sample position. It is difficult to satisfy this requirement at a third-generation source like the Advanced Photon Source (APS). Area-detector pixels are typically square while the source is very asymmetric. At our beamline at the APS, the full width at half-maximum (FWHM) source sizes are $\sim$19 µm (vertical) and 260 µm (horizontal). With typical sample-to-detector distances of 4–5 m, the optimum pixel sizes are only $\sim$1 µm (vertical) and 15 µm (horizontal). The optimum vertical pixel size is impractically small. Thus to further improve the small-angle XPCS set-up hosted at beamline 8-ID at the APS and concomitantly increase the range of time scales accessible *via* XPCS, we have implemented vertical focusing to utilize the full coherent flux delivered by the undulator.

Coherence-preserving one-dimensional (1-D) focusing can be achieved in a variety of ways such as tangentially focusing mirrors, linear Fresnel zone plates (FZPs) and refractive lenses such as compound refractive lenses (CRLs) or kinoforms. The general advantages of refractive lenses for X-ray focusing are outlined by Suehiro *et al.* (1991). We have decided to use moderate ($\sim$50–100:1) demagnification silicon kinoform refractive lenses (Evans-Lutterodt *et al.*, 2003) primarily because they can be added to the existing beamline set-up at 8-ID in a stable and relatively easy and inexpensive manner. Initially, we have chosen to use higher-order kinoforms because the lateral feature sizes are larger and so are more easily fabricated. A primary disadvantage of kinoform lenses is that they are chromatic, but energy tunability is rarely a

‡ Current address: Petra-III, DESY, Hamburg, Germany.

requirement for hard X-ray PCS experiments. Moreover, specific to beamline 8-ID, we simultaneously operate a fixed-energy (7.35 keV) side station for grazing-incidence small-angle X-ray scattering (GISAXS) so energy changes are rare. We also note that the lenses are compact enough in the focusing direction (∼0.5 mm) that several lenses for a predetermined set of specific energies can be fabricated on a single wafer and selected *via* translation. Alianelli *et al.* (2009), Jark *et al.* (2004) and Aristov *et al.* (2000) describe other recent work directed towards the fabrication and application of state-of-the-art X-ray kinoform lenses. Moreno *et al.* (1997) provide a description of the kinoform profile (at optical wavelengths) and its relationship with and performance compared with different types of zone plates.

The remainder of this paper is organized as follows. §2 describes fabrication of the lenses and the experimental set-ups for characterizing the focusing performance of the lenses and their applicability to XPCS measurements. §3.1 describes characterization of the lenses and §3.2 presents characterization of the speckle with and without the focusing lens and the applicability of the lenses for XPCS. §4 presents our conclusions.

2. Experiment

As shown by Evans-Lutterodt *et al.* (2003), the ideal refracting surface of a kinoform is an ellipse. To an excellent approximation, however, especially for relatively small illuminated apertures compared with the maximum aperture, the refracting surface can be approximated by the more commonly discussed parabolic profile of CRLs (Lengeler *et al.*, 1999) and blazed FZPs. Als-Nielsen & McMorrow (2001) provide a physically intuitive derivation of the parabolic profile of the blazed FZP and explain that the first-order zone boundaries are defined by phase differences through the material that are integer multiples of 2π. The zone boundaries are shown to be located at the transverse positions $(n2\lambda f)^{1/2}$, where n is an integer > 0, λ is the wavelength and f is the focal length. The same reference also points out that the lens gain is increased and the optical performance unchanged when lens material producing additional 2π phase shifts (λ/δ, where δ is the refractive index decrement) is removed. A higher-order FZP is constructed using exactly the same arguments except now the Mth-order zone boundaries, where M is a positive integer, are defined by phase differences through the material that are integer multiples of $2M\pi$ and are located at $(nM2\lambda f)^{1/2}$. Analogous to a first-order optic, the lens gain is increased and the optical performance is unchanged when material producing additional $2M\pi$ phase shifts ($M\lambda/\delta$) is removed. The argument outlined above applies equally to kinoforms. Fig. 1 shows calculated kinoform profiles for first-order (solid lines) and sixth-order (dashed lines) lenses. The calculated profiles are for E = 7.35 keV and a focal length of 0.97 m. For clarity, the lens elements have been shifted to ΔZ = 0 µm. From Fig. 1 we see that the primary advantage of higher-order lenses is that they are more forgiving with respect to lithography and etching procedures (lateral feature sizes are larger) and therefore promise more idealized performance, while the primary disadvantage is increased absorption.

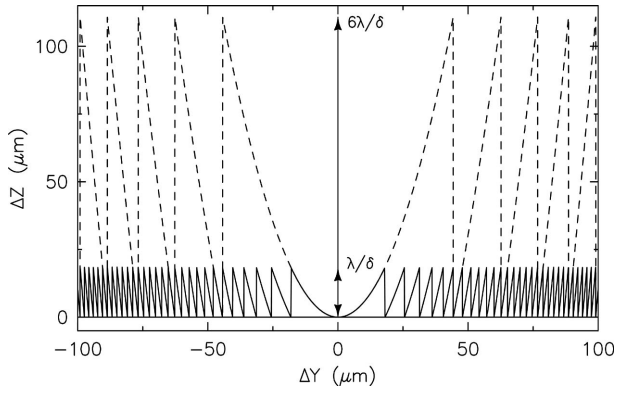

Figure 1
Calculated first-order (solid lines) and sixth-order (dashed lines) kinoform profiles for a silicon lens designed for E = 7.35 keV and f = 0.97 m.

A sixth-order lens (A) and a fifth-order lens (B) were fabricated for the measurements described below. Lens A had a design focal length of 0.97 m while that of lens B was 0.87 m. Both lenses were optimized for 7.35 keV. The lenses were fabricated in silicon *via* e-beam lithography and deep etching (Stein *et al.*, 2008).

Fig. 2 shows a portion of lens A taken through an optical microscope. X-rays are incident from the left and focus to the right in a line orthogonal to the page. The complete lens has 32 zones; eight zones are pictured. The ideal width of the outermost zone is 3.8 µm. The length of the lens along the beam is 3.5 mm. The coordinate system in the figure corresponds to the coordinate system of the beamline: x is horizontal (out of the page), y is vertical and z is along the X-ray-beam direction. The designed vertical aperture of the lens is 500 µm, though the useful aperture was found to be ∼400 µm. The horizontal aperture of lens A (the etch direction) is

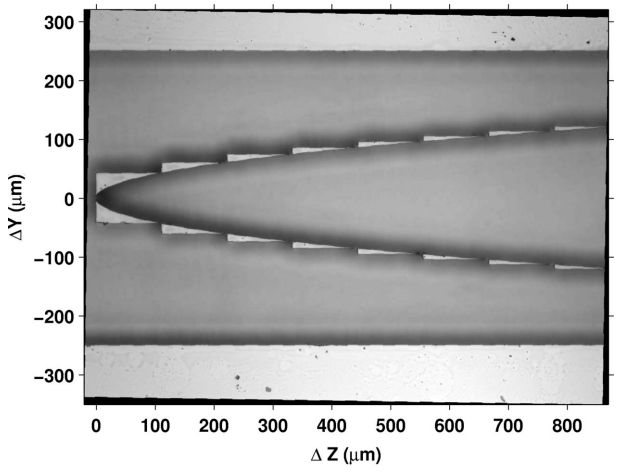

Figure 2
Image of lens A. X-rays are incident from the left and focus to the right in a line orthogonal to the page. Eight of 32 total zones are shown. The etch depth (out of the page) is ∼80 µm.

$\sim$80 μm, though the quality of the lens was qualitatively observed to degrade with etch depth. Lens *B* has similar properties to lens *A* though the etch depth was only $\sim$30 μm and it is a fifth-order lens.

Two types of measurements were made with the lenses. First, the X-ray-beam focusing performance was evaluated by knife-edge scans through the focus. Second, the effect on X-ray speckle and small-angle XPCS measurements was evaluated by comparing static and dynamic speckle patterns obtained with and without a lens focusing the beam at the sample position.

For both types of measurements the beamline configuration upstream of the lens was as follows. A beam from APS undulator A passes through a 275 μm-diameter pinhole 27 m from the source. This beam is deflected 5 mrad inboard by a water-cooled plane silicon mirror 30 m from the source that acts as a low-pass filter. The resulting so-called 'pink beam' is monochromated by a water-cooled artificial channel-cut Ge(111) monochromator (Narayanan *et al.*, 2008) 65 m from the source. The stability and coherence preservation of the beamline has been characterized previously and found to be almost ideal (Sandy *et al.*, 2007; Narayanan *et al.*, 2008), meaning that there are no unknown effective sources or non-ideal optics in the beamline. The first harmonic energy was set to $E_1 = 7.35$ keV which was the design energy of the kinoform lenses. The lenses were placed immediately downstream of the collimating (coherence-selecting) slits, which are 68 m from the source, atop a positioning system that allows for pitch and yaw alignment of the lenses, as well as translation in the *xy* plane.

For focus-size measurements, the lenses and knife-edge were in air. The knife-edge was a 20 nm-thick layer of chromium deposited atop a silicon 'wall' extending from a silicon wafer and was $\sim$2 μm thick along *z*. The chromium *Kα* fluorescence signal was used to characterize the focused X-ray-beam profile.

For speckle and XPCS measurements, the lens was placed in a small vacuum cross atop the aforementioned stages and vacuum integrated with the normal small-angle multi-speckle XPCS set-up at beamline 8-ID (Sandy *et al.*, 2007). Two sets of in-vacuum guard slits near the sample chamber were used to eliminate parasitic small-angle scattering. The two sets of guard slits are part of the standard small-angle coherent-scattering set-up at beamline 8-ID (*i.e.* with or without the lens): the first pair reduces the parasitic scattering produced by the collimating slit, and the second reduces the parasitic scattering produced by the first guard slit. Dual sets of guard slits are especially important for small-angle coherent scattering experiments where the dynamic range of detectors is limited and background cannot be subtracted from the signal (Livet, 2007).

Silica aerogel samples were used to produce static X-ray speckle (Abernathy *et al.*, 1998; Sandy *et al.*, 1999) while concentrated latex spheres of radius 260 nm in a mixture of glycerol and water-cooled to 253 K were used to generate fluctuating X-ray speckle patterns (Lurio *et al.*, 2000). Both samples were contained in a small vacuum chamber which was vacuum integrated with the incident and exit flight paths. At the end of the exit flight path, a tungsten beamstop blocks the transmitted beam.

Static X-ray speckle patterns were measured using a Princeton Instruments LCX-1300 deep-depletion direct-detection CCD detector (PI detector) having 1300×1340 $20\ \mu m \times 20\ \mu m$ pixels. Fluctuating speckle patterns were recorded using a SMD CCD detector especially modified for relatively fast direct X-ray detection (Falus *et al.*, 2004). It has 1024×1024 $14\ \mu m \times 14\ \mu m$ pixels. Static data were analyzed *via* azimuthal and radial averaging and spatial autocorrelations as described previously (Dufresne *et al.*, 1995; Sandy *et al.*, 1999; Abernathy *et al.*, 1998) to yield the small-angle X-ray scattering profile (SAXS) and the speckle amplitudes and widths as a function of wavevector transfer. Dynamic data were analyzed *via* pixel-by-pixel time autocorrelations then azimuthally and radially averaged. The radial bin size for the time autocorrelations, ΔQ, was $\sim$30 pixels or 0.0044 nm^{-1} (which is comparable with the largest speckle widths measured). The effect of radial binning on correlation functions is discussed by Lumma *et al.* (2000).

3. Results and discussion

3.1. Kinoform lens characterization

Open squares in Fig. 3 are the measured vertical profile of the beam focused by lens *A* at the experimentally determined focus position. The focus position was found to be 1.05 m from the lens rather than the design value of 0.97 m. The measured profile consists of a narrow high-amplitude central component with relatively weak wings. The ideal profile, as determined by wave-optic calculations, is shown as a dashed line in Fig. 3. The measured profile shows the same overall features as the ideal profile, namely a relatively sharp central peak and enhanced

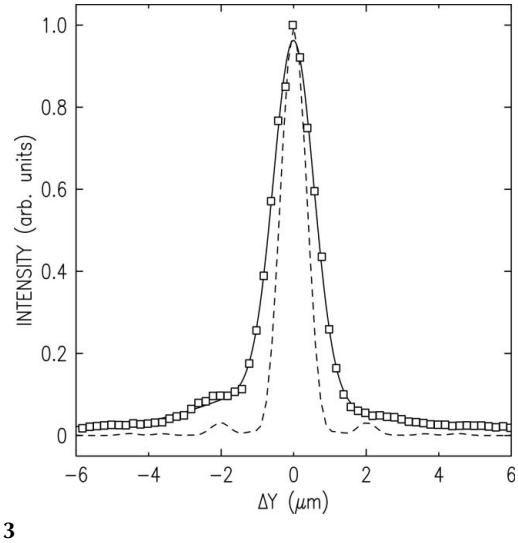

Figure 3
Vertical knife-edge scan at the focus of lens *A*. Open squares are the measured fluorescence intensity and the solid line is the fit described in the text. The dashed line is the expected profile based on wave-optic simulations.

scattering in the wings corresponding to the sinc function that describes the intensity distribution of light in the focal plane of a 1-D optic (Born & Wolf, 1980). The measured profile is, however, broader than expected. To quantify this observation, we have fitted the measured profile to an empirically assigned sum of two Gaussians and a constant background term. The resulting best fit is shown as a solid line in Fig. 3. The fitted 1σ width of the narrow high-amplitude component is 0.54 ± 0.01 μm. This value should be compared with the expected value of 0.34 μm based on the sum in quadrature of the diffraction limit for 1-D focusing [which is given by the Rayleigh criterion $R_{\rm dl} = 0.5\lambda/{\rm NA}$ (Born & Wolf, 1980), where NA is the numerical aperture of the lens] and the source demagnification. The measured focal line width is 63% broader than expected. The focal profile of lens *B* was also measured and yielded a focal line width of $\sigma = 0.52 \pm 0.01$ μm compared with the expected value of 0.30 μm. The design focal length of this lens was 0.87 m and the measured focal length was 0.97 m.

We do not understand the discrepancies between the observed and expected focal line widths and focal lengths. With respect to the focal line widths, we can exclude vibrations of the source, the lens positioning stages or knife-edge vibrations because the same set-up has been used at our beamline to measure focal line widths considerably smaller than the expected values for these lenses. Another possibility, which could be related to the longer than expected focal length, is that the lens is somehow not being used at its optimum X-ray energy despite the fact that it was designed for $E = 7.35$ keV. The beamline energy was fixed for our measurements so we could not investigate this possibility directly but we did perform calculations in which we varied the measurement energy relative to the design energy. A 9% increase in measurement energy linearly increases the focal length from 0.97 to 1.05 m but the calculated focal line width only increases by 3% (though the gain decreases by more than this) so does not account for the observed broadening. We hypothesize that the broadening is the result of errors in the lens fabrication process such as the etch undercutting the lens elements.

We also measured the efficiency and gain of the kinoform lenses, the former being of primary importance for evaluating the overall improvement provided by kinoform lenses to XPCS measurements. The efficiency was measured by computing the ratio of integrated intensities from knife-edge scans with and without the lens. The results of these measurements and the expected and observed properties of the two lenses are summarized in Table 1. For both lenses the efficiency was 33% which is less than the expected value of 41%.

Table 1
Measured, calculated and designed kinoform lens properties at 7.35 keV.

	Lens *A*	Lens *B*
Order	6	5
Design focal length (m)	0.97	0.87
Measured focal length (m)	1.05	0.95
Calculated focus width (μm)	0.94	0.83
Measured focus width (μm)	1.50	1.44
Integrated efficiency (%)	33	33
Gain	46	50

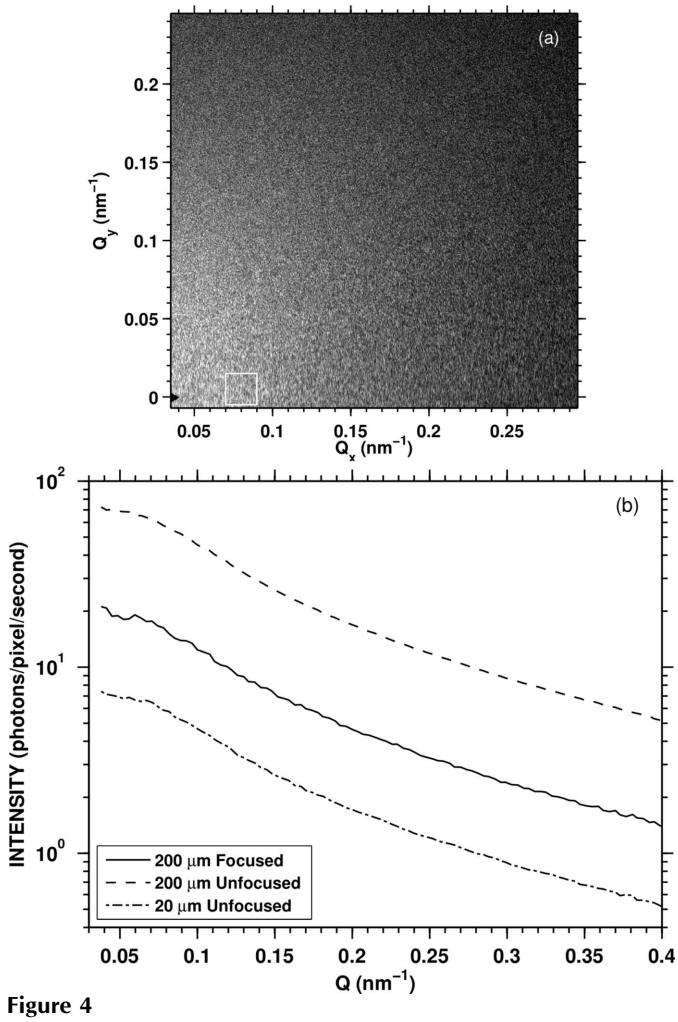

Figure 4
(*a*) Small-angle scattering produced *via* a static disordered aerogel sample illuminated with a vertically focused beam as described in the text. (*b*) Azimuthally averaged small-angle scattering from the above sample under various illumination conditions.

3.2. X-ray speckle characterization

Fig. 4(*a*) shows the two-dimensional small-angle X-ray scattering (SAXS) produced by a static disordered aerogel sample collected by the PI detector and plotted on a logarithmic intensity scale. The sample was illuminated with a beam focused at the sample position *via* lens *B*. The beam incident on the lens was 200 μm in the vertical and 20 μm in the horizontal. Light regions indicate more scattering and dark regions less scattering. The dark triangle at small wavevector transfers is the shadow of the direct beamstop and the white rectangle indicates the region of the CCD that is displayed in Figs. 5(*a*)–5(*c*). The grainy nature of the scattering is speckle arising from the coherence of the beam, meaning that the lens preserves the coherence of the incident beam.

Fig. 4(*b*) shows the normalized azimuthally averaged small-angle-scattering profiles under three illumination conditions

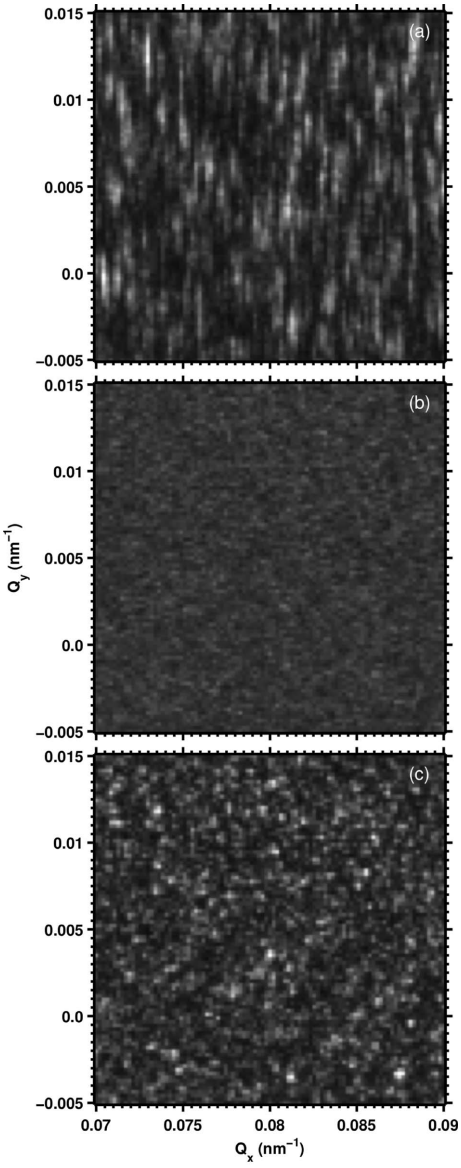

Figure 5
Close-up of the normalized static X-ray speckle patterns produced *via* scattering from an aerogel sample under three illumination conditions: (*a*) 200 µm X-ray beam focused on the sample, (*b*) 200 µm unfocused beam, and (*c*) 20 µm unfocused beam.

plotted as a function of wavevector transfer. In all three cases the horizontal beam aperture was 20 µm. The solid line is the radial intensity profile for the focused beam as above, while the dashed and dot-dashed lines are the radial intensity profiles for 200 µm and 20 µm, respectively, unfocused beams. The only major difference between the SAXS profiles is the overall amplitude of the intensities, which are in the ratio 1.0:0.3:0.1. The fraction 0.1 is the ratio of unfocused beam collimating apertures and the fraction 0.3 is the lens efficiency.

Figs. 5(*a*)–5(*c*) show close-ups of the measured two-dimensional scattering patterns for the three illumination conditions described above. Lighter regions correspond to more scattering and darker regions to less scattering. All three panels have been normalized by the smoothly varying SAXS intensity profile so that the mean intensity of each panel is unity. Most striking is the distinct difference in the speckles between the different panels. In Fig. 5(*a*) the intensity variation of the speckles is large, the number of speckles is relatively small, and the size of the speckles along the vertical (Q_y) direction is large. The relatively small number of speckles is the result of the relatively small illuminated sample area while the large vertical size of the speckles is the result of the small vertical coherence length at the focus (sample position). We emphasize that at the focus the beam is a plane wave (in y) so the large speckle size is not broadening or smearing resulting from the divergence of the beam but rather a finite-size broadening owing to the small coherence length of the beam. In both Figs. 5(*b*) and 5(*c*) considerably more speckles are present and the speckles are much smaller than in Fig. 5(*a*). Also evident is that the intensity variation for the large illuminating aperture (Fig. 5*b*) is considerably less than that for the small illuminating aperture (Fig. 5*c*).

Speckle amplitudes and widths can be quantified by computing the two-point intensity spatial correlation function,

$$C(\mathbf{r}_1, \mathbf{r}_2) = \frac{\langle I(\mathbf{r}_1) I(\mathbf{r}_2) \rangle}{\langle I(\mathbf{r}_1) \rangle \langle I(\mathbf{r}_2) \rangle}, \quad (1)$$

where $\mathbf{r}_i$ are points on the CCD detector plane and the brackets $\langle \ldots \rangle$ denote the spatial average over a suitable detector area. For widely spaced (uncorrelated) points on the detector the autocorrelation is unity. The amplitude of the spatial correlation above unity at $\mathbf{r}_1 = \mathbf{r}_2$ is the speckle contrast, and the width of the decay to the baseline for $|\mathbf{r}_1 - \mathbf{r}_2| > 0$ is the speckle width.

Fig. 6 shows slices along Q_y through the spatial correlations performed on the data sets presented in Fig. 5. Plotted symbols are the calculated autocorrelations and lines are guides for the eye. Two features are evident in Fig. 6. First, the contrast of the focused beam is roughly the same as that from the unfocused 20 µm × 20 µm beam and about seven times

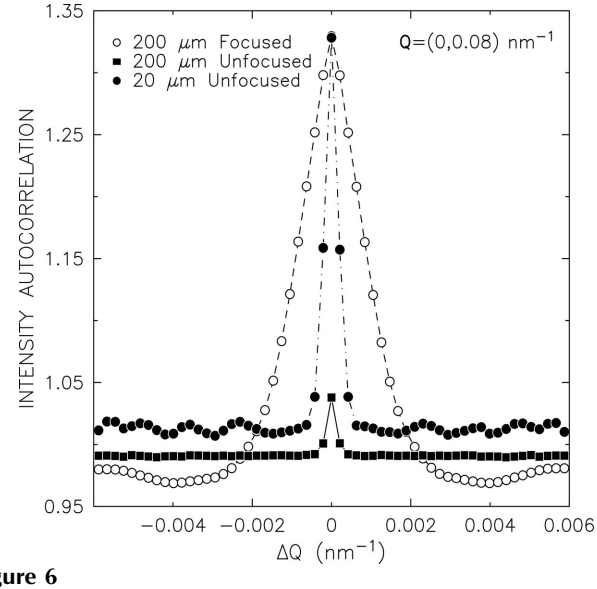

Figure 6
Transverse slices in the Q_y direction through the spatial autocorrelations of the three speckle patterns presented in Fig. 5. Lines are guides for the eye.

greater than that from the unfocused 200 μm × 20 μm beam. Second, the speckle width is considerably greater for the focused beam *versus* the unfocused beam.

With regard to the speckle amplitudes, we observe that focusing with the kinoform lens has preserved or slightly enhanced (because the CCD pixels are no longer oversampling the speckles) the apparent speckle contrast but, importantly, the flux available for coherent scattering experiments (when compared with the unfocused 20 μm × 20 μm beam) has been increased by a factor of three. Since accessible time scales in XPCS experiments scale with the square of the incident flux (Falus *et al.*, 2006), silicon kinoform lenses promise the opportunity to study either dynamics at about ten times faster time scales or to study samples with considerably weaker scattering cross sections.

The greatly increased speckle width in Q_y for the focused beam provides an independent check of the (coherent) vertical extent of the focused beam at the sample. Referring to Fig. 6, we see that for the focused beam the autocorrelation exhibits minima at $Q_y = \pm 0.0040\ \mathrm{nm}^{-1}$. These minima correspond to zeros of the sinc function that describe the focus of a 1-D optic (Born & Wolf, 1980). From the position of the minima, $Q_{\min}$, the vertical size of the focused beam is given by $2\pi/Q_{\min} = 1.57$ μm. This is in reasonable agreement with the knife-edge measurements (1.50 μm) and means that static speckle characterization can be used as an alternate way of measuring focal spot sizes.

A key check is whether the kinoform lenses improve the quality of measured intensity autocorrelation functions. To evaluate this, we have recorded the scattering from the latex sample described in §2 under the three illumination conditions described for Figs. 5(*a*)–5(*c*). For each illumination condition a series of 1024 frames was acquired at 30 frames s^{-1}. Time autocorrelations were calculated *versus* wavevector transfer as described in §2. The top-left inset of Fig. 7 shows the time-averaged small-angle scattering from the sample.

In the low count limit, the SNR for the measured correlation functions is given by (Falus *et al.*, 2006)

$$R_{\mathrm{sn}} = (A-1)/(\mathrm{var}\, g_2)^{1/2} \propto \bar{I}(A-1), \qquad (2)$$

where g_2 is the intensity autocorrelation function, A is the amplitude of the correlation function above the baseline (*i.e.* the contrast or short-time limit of g_2), var is the variance of the measured autocorrelation decay relative to the ideal (or fitted form) and $\bar{I}$ is the mean count rate per pixel. The calculated SNRs *versus* Q relative to the unfocused 20 μm × 20 μm beam are shown as open symbols (focused beam) and solid symbols (200 μm × 20 μm unfocused beam) in Fig. 7. Though there is considerable scatter in the results, the relative SNR is clearly increased for both sets of data at larger Q where the count rate is low. Using the proportionality result in equation (2), we can estimate the expected increase in SNR for the focused and unfocused beams. The relative changes in count rates per pixel are shown in Fig. 4(*b*) while the relative changes in A are obtained from the analysis presented in Fig. 6 or from the short-time limit of the fitted autocorrelation functions. The expected relative SNRs are thus 3 for the focused beam and 1.5 for the large unfocused beam. Solid and dashed lines in Fig. 7 are the measured relative average gains for the focused and unfocused beams for $Q \geq 0.065\ \mathrm{nm}^{-1}$. The measured averages, 3.3 and 2.6, respectively, for the focused and large unfocused beams are in very rough agreement with the predictions and confirm that the kinoform lens increases the quality of the measured correlation functions in comparison with the unfocused beams. We also note that in the case of focusing there is opportunity to further increase this gain by using lower-order lenses with less absorption.

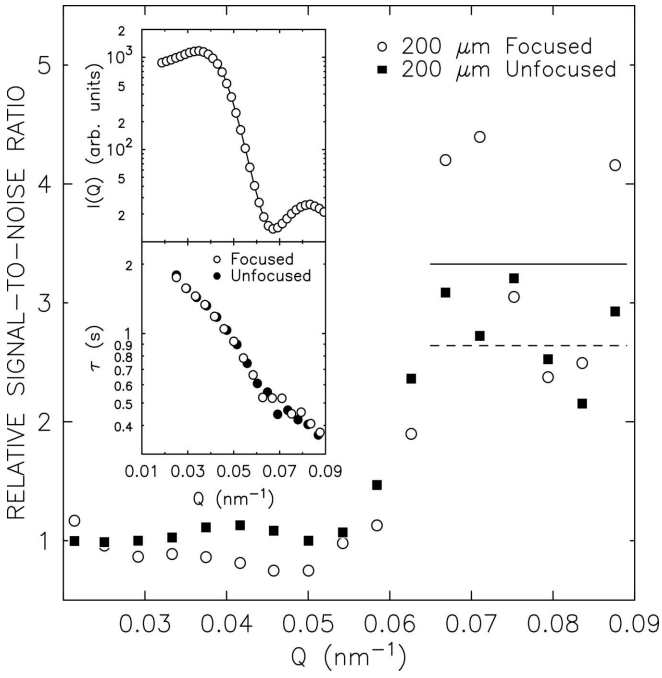

Figure 7
SNRs for measured autocorrelation functions relative to the SNRs for the unfocused 20 μm × 20 μm beam. The top inset shows the time-averaged small-angle scattering measured with the focused beam. The bottom inset shows autocorrelation decay times determined *via* the focused and unfocused beams.

A final verification is whether the same dynamics are measured using the focused beam compared with the relatively small unfocused beam. The lower-left inset of Fig. 7 shows the extracted time constants *versus* Q for correlation functions measured with and without focusing. Time constants measured with the focused beam are shown as open symbols and as solid symbols for the 20 μm × 20 μm unfocused beam. Evidently the use of the focused beam does not affect the measured results.

4. Conclusions

We have successfully fabricated higher-order kinoform lenses in silicon and applied them to small-angle XPCS experiments at the APS. The lenses have good focusing performance achieving vertical focal line widths within 63% of the diffraction limit and have relatively high efficiency even at lower hard X-ray energies, such as 7.35 keV. The demonstrated net gain in usable incident flux for small-angle XPCS experiments is ∼3, which will provide access to faster fluc-

tuation time scales or weaker scatterers. We have also demonstrated that speckle-size characterization can be used to characterize the focusing performance of coherence-preserving X-ray optics.

Our original motivation for making higher-order lenses like those described here was to provide extremely small focused line widths over extended focal line lengths with the aim of assembling crossed kinoform lenses to provide small X-ray focal spots. There is, therefore, significant room to improve kinoform lenses specifically for small-angle XPCS applications where small focusing line widths and large line lengths are not the primary drivers. Specifically, diamond lenses (Nöhammer *et al.*, 2003; Isakovic *et al.*, 2009) or lower-order silicon lenses promise further increases in efficiency and better utilization of the coherent flux delivered by the undulator.

We acknowledge the expert technical assistance of Raymond Ziegler and helpful conversations with Professors Larry Lurio, Simon Mochrie and Mark Sutton. Research carried out in part at the Center for Functional Nanomaterials, Brookhaven National Laboratory, which is supported by the US Department of Energy, Office of Basic Energy Sciences, under Contract No. DE-AC02-98CH10886. Use of the Advanced Photon Source at Argonne National Laboratory was supported by the US Department of Energy, Office of Science, Office of Basic Energy Sciences, under Contract No. DE-AC02-06CH11357.

References

Abernathy, D. L., Grübel, G., Brauer, S., McNulty, I., Stephenson, G. B., Mochrie, S. G. J., Sandy, A. R., Mulders, N. & Sutton, M. (1998). *J. Synchrotron Rad.* **5**, 37–47.

Alianelli, L., Sawhney, K. J. S., Tiwari, M. K., Dolbnya, I. P., Stevens, R., Jenkins, D. W. K., Loader, I. M., Wilson, M. C. & Malik, A. (2009). *J. Synchrotron Rad.* **16**, 325–329.

Als-Nielsen, J. & McMorrow, D. (2001). *Elements of Modern X-ray Physics.* Chichester: Wiley.

Aristov, V., Grigoriev, M., Kuznetsov, S., Shabelnikov, L., Yunkin, V., Weitkamp, T., Rau, C., Snigireva, I., Snigirev, A., Hoffmann, M. & Voges, E. (2000). *Appl. Phys. Lett.* **77**, 4058–4060.

Born, M. & Wolf, E. (1980). *Principles of Optics*, 6th ed. Oxford: Pergamon.

Dufresne, E., Brüning, R., Sutton, M., Rodricks, B. & Stephenson, G. B. (1995). *Nucl. Instrum. Methods Phys. Res. A*, **364**, 380–393.

Evans-Lutterodt, K., Ablett, J., Stein, A., Kao, C.-C., Tennant, D., Klemens, F., Taylor, A., Jacobsen, C., Gammel, P., Huggins, H., Bogart, G., Ustin, S. & Ocola, L. (2003). *Opt. Express*, **11**, 919–926.

Falus, P., Borthwick, M. A. & Mochrie, S. G. J. (2004). *Rev. Sci. Instrum.* **75**, 4383–4400.

Falus, P., Lurio, L. B. & Mochrie, S. G. J. (2006). *J. Synchrotron Rad.* **13**, 253–259.

Grübel, G., Madsen, A. & Robert, A. (2008). *Soft-Matter Characterization*, edited by R. Borsali and R. Pecora. Heidelberg: Springer.

Isakovic, A. F., Stein, A., Warren, J. B., Narayanan, S., Sprung, M., Sandy, A. R. & Evans-Lutterodt, K. (2009). *J. Synchrotron Rad.* **16**, 8–13.

Jark, W., Pérennès, F., Matteucci, M., Mancini, L., Montanari, F., Rigon, L., Tromba, G., Somogyi, A., Tucoulou, R. & Bohic, S. (2004). *J. Synchrotron Rad.* **11**, 248–253.

Lengeler, B., Schroer, C., Tümmler, J., Benner, B., Richwin, M., Snigirev, A., Snigireva, I. & Drakopoulos, M. (1999). *J. Synchrotron Rad.* **6**, 1153–1167.

Livet, F. (2007). *Acta Cryst.* A**63**, 87–107.

Lumma, D., Lurio, L. B., Mochrie, S. G. J. & Sutton, M. (2000). *Rev. Sci. Instrum.* **71**, 3274–3289.

Lurio, L. B., Lumma, D., Sandy, A. R., Borthwick, M. A., Falus, P., Mochrie, S. G. J., Pelletier, J.-F., Sutton, M., Regan, L., Malik, A. & Stephenson, G. B. (2000). *Phys. Rev. Lett.* **84**, 785–788.

Moreno, V., Román, J. F. & Salgueiro, J. R. (1997). *Am. J. Phys.* **65**, 556–562.

Narayanan, S., Sandy, A., Shu, D., Sprung, M., Preissner, C. & Sullivan, J. (2008). *J. Synchrotron Rad.* **15**, 12–18.

Nöhammer, B., David, C., Rothuizen, H., Hoszowska, J. & Simionovici, A. (2003). *Microelectron. Eng.* **67/68**, 453–460.

Sandy, A. R., Jiao, X., Narayanan, S. & Sprung, M. (2007). *AIP Conf. Proc.* **879**, 898–901.

Sandy, A. R., Lurio, L. B., Mochrie, S. G. J., Malik, A., Stephenson, G. B., Pelletier, J. F. & Sutton, M. (1999). *J. Synchrotron Rad.* **6**, 1174–1184.

Stein, A., Evans-Lutterodt, K., Bozovic, N. & Taylor, A. (2008). *J. Vac. Sci. Technol. B*, **26**, 122–127.

Suehiro, S., Miyaji, H. & Hayashi, H. (1991). *Nature (London)*, **352**, 385–386.

Sutton, M. (2008). *C. R. Phys.* **9**, 657–667.